

Three-dimensional and high-speed swept-source optical coherence tomography for *in vivo* investigation of human anterior eye segments

Yoshiaki Yasuno, Violeta Dimitrova Madjarova, Shuichi Makita

Institute of Applied Physics, University of Tsukuba, Tennodai 1-1-1, Ibaraki, Tsukuba, 305-8573, Japan

Masahiro Akiba

Yamagata Promotional Organization for Industrial Technology, 2-2-1 Matsuei, Yamagata, Yamagata, 990-2473, Japan

Atsushi Morosawa, Changho Chong, Toru Sakai

Santec Corporation, Photonics Valley Ohkusa Campus, 5823 Nenjojzaka, Ohkusa, Komaki, Aichi, 485-0802, Japan

Kin-Pui Chan

Yamagata Promotional Organization for Industrial Technology, 2-2-1 Matsuei, Yamagata, Yamagata, 990-2473, Japan

Masahide Itoh and Toyohiko Yatagai

Institute of Applied Physics, University of Tsukuba, Tennodai 1-1-1, Ibaraki, Tsukuba, 305-8573, Japan

yasuno@optlab2.bk.tsukuba.ac.jp

<http://optics.bk.tsukuba.ac.jp/COG/>

Abstract: A two- and three-dimensional swept source optical coherence tomography (SS-OCT) system, which uses a ready-to-ship scanning light source, is demonstrated. The light source has a center wavelength of 1.31 μm , -3 dB wavelength range of 110 nm, scanning rate of 20 KHz, and high linearity in frequency scanning. This paper presents a simple calibration method using a fringe analysis technique for spectral rescaling. This SS-OCT system is capable of realtime display of two-dimensional OCT and can obtain three-dimensional OCT with a measurement time of 2 s. *In vivo* human anterior eye segments are investigated two- and three-dimensionally. The system sensitivity is experimentally determined to be 112 dB. The three-dimensional OCT volumes reveal the structures of the anterior eye segments, which are difficult to observe in two-dimensional OCT images. A two dimensional tomographic movie shows a dynamic motion of a human iris.

© 2005 Optical Society of America

OCIS codes: (170.4500) Optical coherence tomography; (110.6880) Three-dimensional image acquisition; (110.4500) Optical coherence tomography; (170.4470) Ophthalmology

References and links

1. A. F. Fercher and C. K. Hitzenberger and G. Kamp and S. Y. El-Zaiat, "Measurement of intraocular distances by backscattering spectral interferometry," *Opt. Commun.* **117**, 43–48 (1995).
2. Gerd Häusler and Michael Walter Lindner, "Coherence radar" and "spectral radar" —New tools for dermatological diagnosis," *J. Biomed. Opt.* **3**, 21–31 (1998).
3. D. Huang and E. A. Swanson and C. P. Lin, J. S. Schuman, W. G. Stinson and W. Chang and M. R. Hee, T. Flotte and K. Gregory and C. A. Puliafito and J. G. Fujimoto, "Optical coherence tomography," *Science* **254**, 1178–1181 (1991).
4. W. Drexler and U. Morgner and F. X. Kartner and C. Pitris and S. A. Boppart and X. D. Li and E. P. Ippen and J. G. Fujimoto, "In vivo ultrahigh-resolution optical coherence tomography," *Opt. Lett.* **24**, 1221–1223 (1999).
5. B. Povazay and K. Bizheva and A. Unterhuber and B. Hermann and H. Sattmann and A. F. Fercher and W. Drexler and A. Apolonski and W. J. Wadsworth and J. C. Knight and P. St. J. Russell and M. Vetterlein and E. Scherzer, "Submicrometer axial resolution optical coherence tomography," *Opt. Lett.* **27**, 1800–1802 (2002).
6. R. A. Leitgeb, W. Drexler, A. Unterhuber, B. Hermann, T. Bajraszewski, T. Le, A. Stingl and A. F. Fercher, "Ultrahigh resolution Fourier domain optical coherence tomography," *Opt. Express* **12**, 2156–2165 (2004), <http://www.opticsexpress.org/abstract.cfm?URI=OPEX-12-10-2156>.
7. Maciej Wojtkowski, Vivek J. Srinivasan, Tony H. Ko, James G. Fujimoto, Andrzej Kowalczyk and Jay S. Duker, "Ultrahigh-resolution, high-speed, Fourier domain optical coherence tomography and methods for dispersion compensation," *Opt. Express* **12**, 2404–2422 (2004), <http://www.opticsexpress.org/abstract.cfm?URI=OPEX-12-11-2404>.
8. Barry Cense, Nader A. Nassif, Teresa C. Chen, Mark C. Pierce, Seok-Hyun Yun, B. Hyle Park, Brett E. Bouma, Guillermo J. Tearney and Johannes F. de Boer, "Ultrahigh-resolution high-speed retinal imaging using spectral-domain optical coherence tomography," *Opt. Express* , **12**, 2435–2447 (2004), <http://www.opticsexpress.org/abstract.cfm?URI=OPEX-12-11-2435>.
9. Maciej Wojtkowski, Tomasz Bajraszewski, Piotr Targowski and Andrzej Kowalczyk, "Real-time *in vivo* imaging by high-speed spectral optical coherence tomography," *Opt. Lett.* **28**, 1745–1747 (2003).
10. N. A. Nassif, B. Cense, B. H. Park, M. C. Pierce, S. H. Yun, B. E. Bouma, G. J. Tearney, T. C. Chen and J. F. de Boer, "In vivo high-resolution video-rate spectral-domain optical coherence tomography of the human retina and optic nerve," *Opt. Express* **12**, 367–376 (2004), <http://www.opticsexpress.org/abstract.cfm?URI=OPEX-12-3-367>.
11. Takahisa Mitsui, "Dynamic range of optical reflectometry with spectral interferometry," *Jpn. J. Appl. Phys.* **38**, 6133–6137 (1999).
12. R. A. Leitgeb, C. K. Hitzenberger, A. F. Fercher, "Performance of fourier domain vs. time domain optical coherence tomography," *Opt. Express* **11**, 889–894 (2003), <http://www.opticsexpress.org/abstract.cfm?URI=OPEX-11-8-889>.
13. Johannes F. de Boer, Barry Cense, B. Hyle Park, Mark C. Pierce, Guillermo J. Tearney and Brett E. Bouma, "Improved signal-to-noise ratio in spectral-domain compared with time-domain optical coherence tomography," *Opt. Lett.* **28**, 2067–2069 (2003).
14. Michael A. Choma, Marinko V. Sarunic, Changhuei Yang and Joseph A. Izatt, "Sensitivity advantage of swept source and Fourier domain optical coherence tomography," *Opt. Express* **11**, 2183–2189 (2003), <http://www.opticsexpress.org/abstract.cfm?URI=OPEX-11-18-2183>.
15. S. R. Chinn, E. A. Swanson and J. G. Fujimoto, "Optical coherence tomography using a frequency-tunable optical source," *Opt. Lett.* **22**, 340–342 (1997).
16. S. H. Yun, C. Boudoux, G. J. Tearney and B. E. Bouma, "High-speed wavelength-swept semiconductor laser with a polygon-scanner-based wavelength filter," *Opt. Lett.* **28**, 1981–1983 (2003).
17. S. H. Yun, G. J. Tearney, J. F. de Boer, N. Iftimia and B. E. Bouma, "High-speed optical frequency-domain imaging," *Opt. Express* **11**, 2953–2963 (2003), <http://www.opticsexpress.org/abstract.cfm?URI=OPEX-11-22-2953>.
18. R. Huber, M. Wojtkowski, K. Taira, J. G. Fujimoto and K. Hsu, "Amplified, frequency swept lasers for frequency domain reflectometry and OCT imaging: design and scaling principles," *Opt. Express* **13** 3513–3528 (2005), <http://www.opticsexpress.org/abstract.cfm?URI=OPEX-13-9-3513>.
19. S. H. Yun, G. J. Tearney, J. F. de Boer and B. E. Bouma, "Motion artifacts in optical coherence tomography with frequency-domain ranging," *Opt. Express* **12**, 2977–2998 (2004), <http://www.opticsexpress.org/abstract.cfm?URI=OPEX-12-13-2977>.
20. S. H. Yun, G. J. Tearney, J. F. de Boer and B. E. Bouma, "Removing the depth-degeneracy in optical frequency domain imaging with frequency shifting," *Opt. Express* **12**, 4822–4828 (2004), <http://www.opticsexpress.org/abstract.cfm?URI=OPEX-12-20-4822>.
21. Jun Zhang, Woonggyu Jung, J. Stuart Nelson and Zhongping Chen, Full range polarization-sensitive Fourier domain optical coherence tomography, *Opt. Express* **12**, 6033–6039 (2004), <http://www.opticsexpress.org/abstract.cfm?URI=OPEX-12-24-6033>.

22. Jun Zhang, J. Stuart Nelson and Zhongping Chen, "Removal of a mirror image and enhancement of the signal-to-noise ratio in Fourier-domain optical coherence tomography using an electro-optic phase modulator," *Opt. Lett.* **30**, 147–149(2005).
23. M. Wojtkowski, A. Kowalczyk, R. Leitgeb, and A. F. Fercher, "Full range complex spectral optical coherence tomography technique in eye imaging," *Opt. Lett.* **27**, 1415–1417 (2002).
24. Rainer A. Leitgeb, Christoph K. Hitzenberger, Adolf F. Fercher, and Tomasz Bajraszewski, "Phase-shifting algorithm to achieve high-speed long-depth-range probing by frequency-domain optical coherence tomography," *Opt. Lett.* **28**, 2201–2203 (2003).
25. Yoshiaki Yasuno, Shuichi Makita, Takashi Endo, Gouki Aoki, Hiroshi Sumimura, Masahide Itoh, and Toyohiko Yatagai, "One-shot-phase-shifting Fourier domain optical coherence tomography by reference wavefront tilting," *Opt. Express* **12**, 6184–6191 (2004), <http://www.opticsexpress.org/abstract.cfm?URI=OPEX-12-25-6184>.
26. Erich Götzinger, Michael Pircher, Rainer A. Leitgeb, and Christoph K. Hitzenberger, "High speed full range complex spectral domain optical coherence tomography," *Opt. Express* **13**, 583–594 (2005), <http://www.opticsexpress.org/abstract.cfm?URI=OPEX-13-2-583>.
27. Marinko V. Sarunic, Michael A. Choma, Changhui Yang, and Joseph A. Izatt, "Instantaneous complex conjugate resolved spectral domain and swept-source OCT using 3x3 fiber couplers," *Opt. Express* **13**, 957–967 (2005), <http://www.opticsexpress.org/abstract.cfm?URI=OPEX-13-3-957>.
28. Yoshiaki Yasuno, Shuichi Makita, Takashi Endo, Gouki Aoki, Masahide Itoh, and Toyohiko Yatagai, "Simultaneous B-M-mode scanning method for realtime full-range Fourier domain optical coherence tomography," *Appl. Opt.* (accepted to publication).
29. Mitsuo Takeda, Hideki Ina and Seiji Kobayashi, "Fourier-transform method of fringe-pattern analysis for computer-based topography and interferometry," *J. Opt. Soc. Am.* **72**, 156–160 (1982).
30. Christophe Dorrer, Nadia Belabas, Jean-Pierre Likhoman, and Manuel Joffre, "Spectral resolution and sampling issues in Fourier-transform spectral interferometry," *J. Opt. Soc. Am. B* **17**, 1795–1802 (2000).
31. Maciej Wojtkowski, Rainer Leitgeb, Andrzej Kowalczyk, Tomasz Bajraszewski, and Adolf F. Fercher, "In vivo human retinal imaging by Fourier domain optical coherence tomography," *J. Biomed. Opt.* **7**, 457–463 (2002).
32. Jun Zhang and Zhongping Chen, "In vivo blood flow imaging by a swept laser source based Fourier domain optical Doppler tomography," *Opt. Express* **13**, 7449–7457 (2005), <http://www.opticsexpress.org/abstract.cfm?URI=OPEX-13-19-7449>.
33. Michael A. Choma, Kevin Hsu, and Joseph A. Izatt, "Swept source optical coherence tomography using an all-fiber 1300-nm ring laser source," *J. Biomed. Opt.* **10**, 044009 (2005).
34. B. J. Vakoc, S. H. Yun, J. F. de Boer, G. J. Tearney, and B. E. Bouma, "Phase-resolved optical frequency domain imaging," *Opt. Express* **13**, 5483–5493 (2005), <http://www.opticsexpress.org/abstract.cfm?URI=OPEX-13-14-5483>.
35. Anjul M. Davis, Michael A. Choma, and Joseph A. Izatt, "Heterodyne swept-source optical coherence tomography for complete complex conjugate ambiguity removal," *J. Biomed. Opt.* **10**, 064005 (2005).
36. American National Standards institute, "American National Standard for the Safe Use of Lasers ANSI Z136.1-2000," American National Standards institute, New York (2000).

1. Introduction

Fourier domain optical coherence tomography (FD-OCT) or spectral domain optical coherence tomography (SD-OCT)[1, 2], which was first demonstrated around the mid-1990s, is a promising alternative to time domain optical coherence tomography (TD-OCT)[3]. The resolution of OCT, including either TD-OCT or FD-OCT, is higher than that of X-ray tomography or magnetic resonance imaging (MRI). A few-micron or sub-micron depth resolutions has been demonstrated using solid state lasers and semiconductor light sources[4, 5, 6, 7, 8].

The measurement speed of SD-OCT is higher than that of TD-OCT because of the absence of mechanical depth scanning (A-scan). In SD-OCT, the mechanical A-scan has been eliminated by a wavelength-resolving detection scheme using a high-speed spectrometer. Realtime[9] and video-rate[10] SD-OCT systems have been demonstrated. Another major advantage of SD-OCT systems over TD-OCT systems is its sensitivity, that has been theoretically proved and experimentally confirmed[11, 12, 13, 14].

Although SD-OCT is a booming technology for 830 nm OCT, it is difficult to apply SD-OCT to 1.3 μm OCT systems. This is because, for the 1.3 μm band, the options available for the line detectors of the high-speed spectrometer are limited, while there are several options for the 830 nm band.

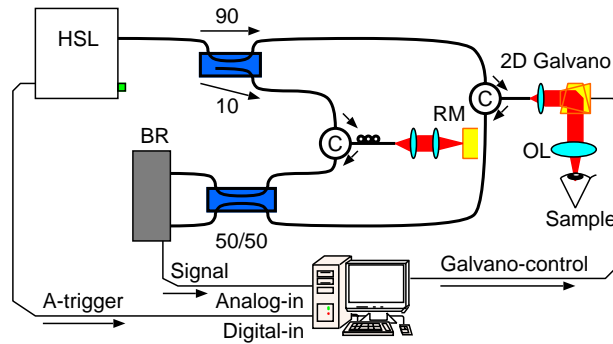


Fig. 1. The optical scheme of SS-OCT. HSL: high-speed wavelength scanning light source, C: circulator, RM: reference mirror, OL: objective, and BR: balanced photo receiver.

For 1.3 μm band, swept-source optical coherence tomography (SS-OCT), which is a variation of FD-OCT, is a good alternative to SD-OCT. SS-OCT detects the wavelength-resolved interference signal by using an instantaneously monochromatic but wavelength scanning laser source and a point photo detector, while SD-OCT detects the wavelength-resolved interference signal by using a spectrometer consisting of a diffraction grating, Fourier transform lens, and a detector array or a line-scan camera. Although, SS-OCT has been known as optical frequency domain reflectometry and has a long history, it is only in recent years that the SS-OCT has been performed as tomography[15]. Since the development of the fast scanning light source[16], SS-OCT has been applied for high-speed *in vivo* tomographic measurements[17]. Recently, SS-OCT systems whose measurement speeds are comparable to or faster than 830 nm SD-OCT have been demonstrated[17, 18].

Since SS-OCT is a variation of FD-OCT, similar to SD-OCT, it maintains its advantage of sensitivity over TD-OCT[14, 17]. Furthermore, SS-OCT has several major advantages over SD-OCT. One advantage is its higher robustness against sample motions than SD-OCT because of its short exposure time and imaging mechanism[19]. The other advantage is its capability of separating the real OCT image from its mirror image[20, 21, 22], in contrast SD-OCT requires several measurements or an elaborate optical setup to eliminate its mirror images[23, 24, 25, 26, 27, 28].

For our SS-OCT system, we employed a ready-to-ship wavelength scanning light source with an A-scan rate of 20 KHz, a light output duty cycle exceeding 50%, high frequency linearity in scanning time, and it provides alignment-free-stability and turn-key operation. This SS-OCT system does not use a k-trigger[20, 21, 18], but a simple calibration method to rescale the spectrum into linear frequency space. This calibration method uses a phase oriented fringe analysis technique[29] and does not require any additional equipment, such as a fiber Fabry-Perot interferometer and a fast oscilloscope. This SS-OCT is capable of two-dimensional OCT measurements with an A-scan rate of 20 KHz and three-dimensional OCT measurement with a measurement speed of 2 s/volume for $200 \times 200 \times 1024$ voxels. It is applied in the investigation of *in vivo* anterior eye segments, and it reveals three-dimensional structures such as trabecular meshwork, crystalline lens, nucleus lentis, and vitreous bodies. A two-dimensional tomographic movie is also demonstrated to show a dynamic motion of a human iris.

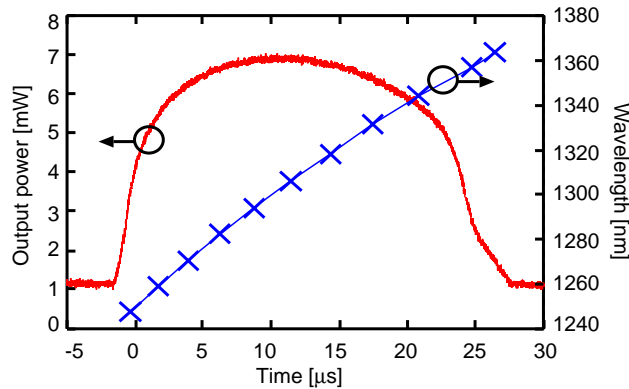


Fig. 2. The instantaneous output power (red curve) and wavelength (blue curve) of the light source. Since the light output duty cycle is 50%, the light emits for 25 μs , then is suppressed for 25 μs .

2. System description

2.1. System basis

Figure 1 shows the scheme of our SS-OCT. The light source is a ready-to-ship scanning light source (HSL-2000, Ver. 1.0, Santec) that has a scanning rate of 20 KHz, light output duty cycle exceeding 50%, -3-dB single-path coherence length of 6 mm, central wavelength of 1.31 μm and -3-dB bandwidth of 110 nm, resulting in a theoretical depth resolution of 6.9 μm in air. The light source consists of a fiber ring cavity with a semiconductor optical amplifier (SOA1016, Kamelian, UK) as a gain medium and a grating (1300 lp/mm) -based external cavity with a polygon scanner for wavelength scanning. The external cavity employs beam expanders to enable a wide tuning range and a narrow instantaneous bandwidth, and further optimization of the external cavity configuration will improve the light output duty cycle. The output wavelength scans as a positive saw-tooth wave from shorter to longer wavelength as shown in Fig. 2. The output beam is introduced into a fiber based Mach-Zehnder interferometer comprising a 10/90 coupler, two identical circulators, and a 50/50 coupler. The second port of one of the circulators is attached to a probe unit, which comprises a fiber collimator lens (11 mm focal length, Thorlabs, Inc.), two-axis galvano mirror (Cambridge Technology), and an achromatic doublet objective with the focal length of 60 mm (Thorlabs, Inc.). The second port of the other circulator is attached to a reference unit comprising a collimator lens, an achromatic doublet Linnik lens and a static gold protected mirror.

The probe and reference beams are re-coupled by the 50/50 coupler and detected by an In-GaAs balanced photo detector with a quantum efficiency of 0.85 (PDA10BI, Thorlabs, Inc.). The balanced photo current, i.e., the spectral interference signal, is converted into voltage, amplified by a factor of 25 by an RF pre-amplifier (SR440, Stanford Research Systems) and sampled by an analog-to-digital (A/D) converter (PXI-9820, ADLINK Technology, Inc.) built in a PXI PC unit with a 14-bit resolution and a sampling rate of 60 MHz. The detected interference signal is rescaled to the linear frequency domain by using the rescaling parameters determined by a simple calibration method described in section 2.2.1. This signal is Hamming windowed, zero-filled from 1700 point sample-length to 2048 point-sample length, and digitally inverse Fourier transformed to yield a single A-scan signal which has 1024 data points. The detection and signal processing are performed by a LabVIEW program.

The half depth measurement range of SS-OCT is determined as

$$\delta z = N\lambda_c^2/4\delta\lambda \quad (1)$$

where λ_c is the center wavelength, $\delta\lambda$ is the wavelength scanning range during the sampling, and N is the number of sampling points. The parameters of our setup, $\lambda_c = 1.31 \mu\text{m}$, $\delta\lambda = 120 \text{ nm}$, and $N = 1700$, result in a depth measurement range of 6.1 mm, which is in good agreement with the experimentally determined measurement range of 6 mm.

2.2. Calibration of frequency linearity

2.2.1. Method

The time dependency of the wavelength of the light source needs to be known in order to determine the rescaling parameters. In order to determine this dependency, we introduced a simple calibration method based on a phase oriented fringe analyzing technique[29]. In this method, a spectral interference signal with a plane mirror sample is measured by SS-OCT. The signal photo current is

$$i_m(t) = 2\eta\Gamma(|z_0|)\sqrt{P_r(t)P_p(t)}\cos\left\{\frac{4\pi}{c}z_0v(t)\right\} \quad (2)$$

where z_0 denotes the path length difference of the interferometer, η photo-detector quantum efficiency, Γ the coherence function of the light source, P_r and P_p optical powers of reference and probe beams, respectively, c speed of light and $v(t)$ instantaneous source optical frequency. The photo-current is digitized in the same manner that in SS-OCT detection, as described in section 2.1, and digitally Fourier transformed as

$$\begin{aligned} \mathfrak{F}[i_m(t)] = \eta\Gamma(|z_0|)\mathfrak{F}\left[\sqrt{P_r(t)P_p(t)}\right] \\ * \left\{ \mathfrak{F}\left[\exp\left(i\frac{4\pi}{c}z_0v_\Omega(t)\right)\right] * \delta\left(\mu - \frac{2}{c}z_0v_1\right) \right. \\ \left. + \mathfrak{F}\left[\exp\left(-i\frac{4\pi}{c}z_0v_\Omega(t)\right)\right] * \delta\left(\mu + \frac{2}{c}z_0v_1\right) \right\} \quad (3) \end{aligned}$$

where $\mathfrak{F}[\cdot]$ denotes the Fourier transform operator, $*$ convolution operator, μ Fourier conjugate of t , and $v(t)$ has been expanded as $v(t) = v_1t + v_\Omega(t)$. The convolved delta-functions of the first and second terms of Eq. (3) are responsible for their appearance at $\mu = \pm 2/cz_0v_1$. This equation shows only two terms. However, in practice, two additional auto correlation terms corresponding to the reference and probe beams exist around the zero-frequency point of the Fourier domain because of the imperfectness of the common-mode rejection of the balanced photo detector. In this calibration process, only the first term in Eq. (3) is clipped out by a flat-top window and inverse-Fourier transformed into the original domain as

$$i'_m(t) = \eta\Gamma(|z_0|)\sqrt{P_r(t)P_p(t)}\exp\{i4\pi z_0v(t)/c\}. \quad (4)$$

This equation and the corresponding measured unwrapped phase yield the following equation;

$$v(t_j) = \frac{c}{4\pi z_0}\phi_m(t_j). \quad (5)$$

where t_j is the time instant of the j -th sampling point and $\phi_m(t_j)$ is the measured unwrapped phase of the j -th sampling point, which is obtained by the above-mentioned procedure. $\phi_m(t_j)$ is

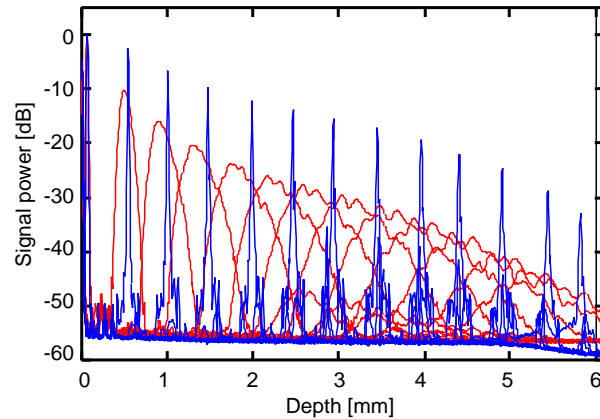


Fig. 3. Point spread functions obtained at several different depth positions. Blue and red curves represent point spread functions with and without rescaling respectively.

fitted by a third order polynomial with the independent variable v and the dependent variable t . This fitting procedure finally gives us the calibration coefficients $a_{0..3}$ of the following equation

$$t(v) \simeq a_0 + a_1v + a_2v^2 + a_3v^3. \quad (6)$$

Finally, this equation and a zero-filling interpolation[30] or fast linear interpolation provide a frequency-linear interference signal.

Figure 3 shows point spread functions (PSFs) at several depth positions. The blue and red curves respectively represent the PSFs with and without above-mentioned frequency rescaling. It is clear that our frequency rescaling technique is very effective in suppressing the depth-dependent resolution decay.

The long-term stability of this calibration method is depend on the long-term stability of the lightsource. In our system, once calibration coefficients are determined, they are applicable for a few month at least. The total calibration time is a few minutes mostly for manual software operation and net calculation time is 170 ms with a 2.0 GHz Pentium M processor on a PXI PC unit (PXI-3800, ADLINK Technology, Inc.) . It is sufficiently short because we need this calibration only once for a few month. On the other hand, frequency-linear-rescaling process is required for every A-scan as same as other calibrations methods of SS-OCT[20, 21, 22] or a spectrometer-based SD-OCT[31, 10]. The fast linear interpolation rescaling algorithm takes 0.3 ms/A-scan (or 150 ms/B-scan containing 500 A-scans), and the zero-filling interpolation takes 2 ms/A-scan (or 1 s/B-scan).

2.2.2. Comparison of calibration and rescaling methods

In recent publications, several types of frequency calibration methods for SS-OCT were demonstrated.

One of these calibration methods is a simultaneous frequency monitoring method[21, 22, 32] in which a small portion of light is introduced into a fiber Fabry-Perot (FFP) interferometer, and the output of the FFP is simultaneously detected and stored with a spectral interference signal. The intensity peaks of the FFP output are utilized as a measure of frequency, and rescaling parameters are derived from this FFP output for each A-scan. Consequently, a rescaling algorithm rescales the interference signal into a frequency linear space by using the rescaling parameters. This method has a high phase stability, and a polarization sensitive SS-OCT system has been demonstrated by this calibration method[21]. The phase stability is further improved

by using a phase-reference signal, and Doppler SS-OCT with a phase stability of 1.77 degrees was demonstrated[32]. Despite the high phase stability, this method requires simultaneous two channel signal detection; one channel is for the interference signal and the other is for the FFP output. This two-channel signal detection requires a high-end A/D converter and a large memory space to store the two signals. It is also a drawback of this method that the FFP is relatively expensive.

The frequency even clock method[27, 33, 34, 35] is similar to the simultaneous frequency monitoring method, but in this method the output from an FFP or a fiber Brag grating (FBG) is monitored by a photo detector and converted to a TTL pulse train. The TTL pulse train is introduced into an A/D converter, which detects an interference signal, as a sampling clock. It has been reported that excellent phase stability was achieved by the combination of this method with the phase-reference method[34]. It is noteworthy that this method does not store the FFP/FBG output in the memory and does not require numerical rescaling; this is because the interference signal is frequency-linearly sampled. However, an FFP/FBG is still required and relatively expensive.

Huber *et al.* demonstrated a fast calibration and rescaling algorithm by using an FFP and a nearest neighbor check algorithm[18]. In this method, the output of the FFP is sampled with an almost Nyquist-limited sampling frequency, and the nearest neighbor check algorithm is applied to determine the frequency-even sampling points. According to the positions of the even sampling point, some bins of a simultaneously acquired interference signal are selected to form a frequency-linearly sampled data-set. In this method, an elaborate algorithm is not used for calibration and rescaling; hence, it is capable of high-speed rescaling although two-channel detection and an FFP device are still required.

An unbalanced interferometer and a zero crossing point detection algorithm are also applicable for the calibration process[20]. This method does not use an FFP or an FBG. Alternatively, it uses an unbalanced interferometer, and the output signal is detected by an oscilloscope. From the zero crossings of the interference signal, a set of calibration parameters is derived. Although in this method, neither an FFP nor an FBG is used, requires an additional measurement device, oscilloscope.

Our calibration method, described in section 2.2.1, requires neither FFP/FBG nor an additional measurement device. The calibration signal is generated by an unbalanced interferometer, i.e., an OCT interferometer with a plane mirror sample, and detected by the OCT detection system. Despite its simplicity, this method sacrifices the phase stability of OCT signals because it ignores the instability of wavelength scanning of individual A-scans. The phase stability of our system is approximately 40 degrees. Although this phase stability is not sufficient for phase-sensitive SS-OCT such as polarization sensitive SS-OCT or Doppler SS-OCT, it is sufficient for phase-insensitive SS-OCT imaging.

2.3. Point spread functions

A representative of a point spread function at the depth of 1 mm from the zero-delay point is shown in Fig. 4. Although small sidelobes are visible, they do not significantly degrade OCT images as is shown in Fig. 6. Error in the frequency-calibration algorithm and zero-filling interpolation, and the departure of spectral shape of the light source from Gaussian may account for the sidelobes.

The depth dependence of longitudinal resolution is shown in Fig. 5. The mean resolution within 2 mm depth range is 11.7 μm , while theoretical resolution with Gaussian spectrum is 6.9 μm . The calibration error of the frequency linearity, the departure of the spectral shape from Gaussian (see Fig. 2), and a Hamming window applied to the spectrum before DFT may account for the degradation of the depth resolution.

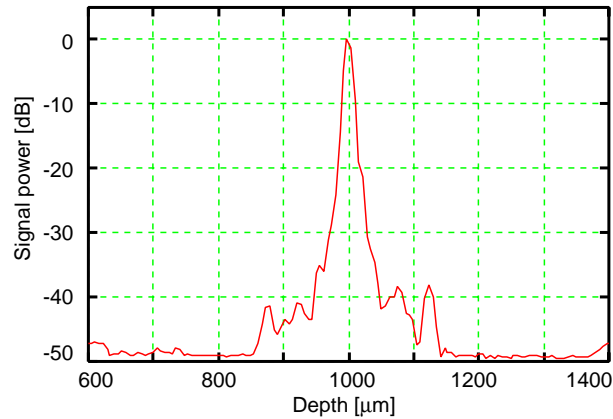


Fig. 4. A representative of point spread functions at the depth of 1 mm.

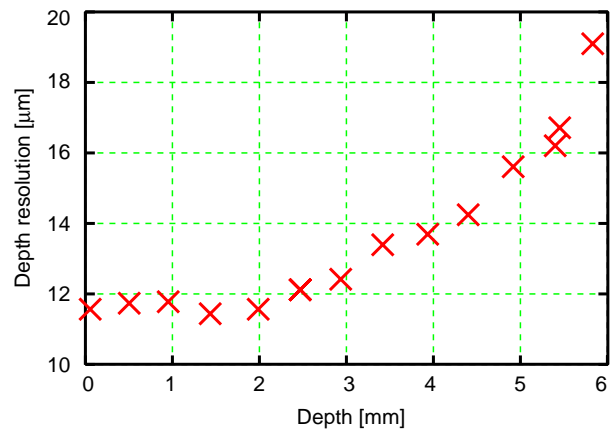


Fig. 5. The depth dependence of longitudinal resolution.

2.4. Sensitivity

The sensitivity of this SS-OCT system is experimentally determined as 112 dB with a probe power of 2.9 mW and -47 dB partially reflecting mirror, while the shot-noise-limited sensitivity is 119 dB. The system loss of 7 dB may account for the following; optical losses such as losses in the back-coupled light into the fiber interferometer and losses in FC/APC attachments, unoptimized magnification of RF pre-amplification, remaining signal RIN, thermal noise of the detector, and circuit noise.

The depth dependence of the sensitivity is evident from Fig. 3. Sensitivity drops -10 dB at the depth point of 1.8 mm, and drops -16 dB at the middle of the measurement range. The limited coherence length of the light source and the errors in frequency rescaling may account for this depth-dependent signal decay.

3. Two-dimensional tomography

In two-dimensional tomography, the galvano mirror in the probe arm is driven by a sawtooth wave. That is synchronously generated with a B-scan trigger by a function generator board

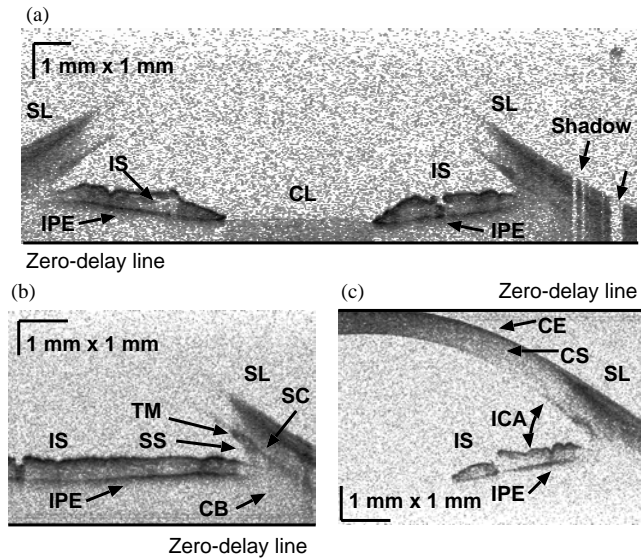


Fig. 6. Two-dimensional tomographies of human anterior eye segments *in vivo*. SL: sclera, IS: iris stroma, IPE: iris pigment epithelium, CL: crystalline lens, SS: scleral spur, TM: trabecular meshwork, SC: Schlemm's canal, CB: ciliary body, CE: corneal epithelium, CS: corneal stroma, and ICA: iridocorneal angle opening. The shadowing lines on the right side of image (a) are because of eyelashes.

(PXI-2502, ADLINK Technology, Inc.) built in a PXI PC unit, and the B-scan trigger triggers the signal sampling of the A/D board. The entire signals for a single B-scan is continuously detected and stored in an on-board buffer of the A/D board. The rotation angle of a polygon scanner in the wavelength tuner of the light source is monitored by a built-in photo diode, whose output initiates a TTL A-scan trigger. The A-scan triggers are simultaneously sampled with the spectral signal by a digital input channel of the A/D converter and utilized to reconstruct a two-dimensional spectral signal from a time sequence of the spectral interference signal. In the detection process, the digitized signal intensity is stored in the first 14-bits of a 2-byte memory space, and the A-scan trigger is stored in the 16th bit of the same 2-byte memory space. Hence, the storage of A-scan trigger involves no memory loss. A typical single B-scan contains 512 A-scans, hence, the acquisition time of a single B-scan is 25.6 ms.

In the realtime measurement mode, which involves data acquisition, spectral rescaling by fast linear interpolation, and Fast Fourier Transform (FFT), the two-dimensional OCT image is displayed with a frame rate of a few frames/s depending on the image size. In this mode, we can interactively and seamlessly adjust the lateral measurement position and range from a software console.

Figures 6(a)-(c) show the tomographies of an *in vivo* human anterior eye segment. Several anatomic features are visible on Figs. 6(a) and 6(b) including sclera (SL), iris stroma (IS), iris pigment epithelium (IPE), crystalline lens (CL), scleral spur (SS), trabecular meshwork (TM), Schlemm's canal (SC) and ciliary body (CB). Although the corneal structures are not visible in Figs. 6(a) and 6(b) because of the depth-dependent sensitivity decay, the optimization of the zero-delay line makes these structures visible as shown in Fig. 6(c). The corneal epithelium (CE) and corneal stroma (CS) are evident in Fig. 6(c). To the best of our knowledge, this is the first time to visualize the full depth of anterior eye chamber, e.g., from the top of the cornea to bottom of the iris, by high-speed SS-OCT. The iridocorneal angle opening (ICA) and the

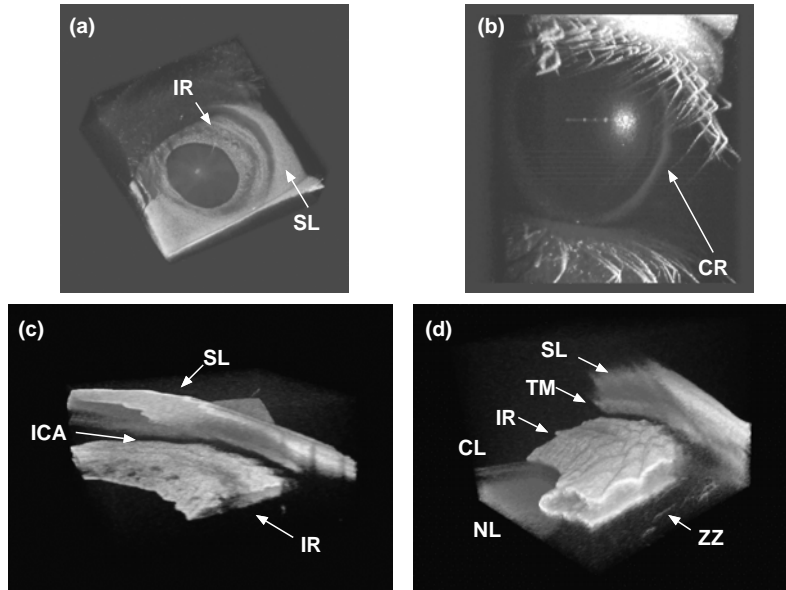


Fig. 7. Three-dimensional tomographies of the human anterior eye segments *in vivo*. (a) sclera and iris (1.8MB), (b) Palpebras and cornea (1.9MB), (c) iridocorneal angle opening (1.6MB), and (d) Iris, crystalline lens, and zonules of Zinn (2.2MB). IR: iris, NL: nucleus lentis, and ZZ: zonules of Zinn.

curvature of the cornea are also evident in these figures. The probe power of these measurements was 2.9 mW, which is well below the ANSI safety standard[36].

4. Three-dimensional tomography

In three-dimensional tomography, the galvano mirror for the B-scan is driven by a triangular wave. A B-scan trigger, which is synchronously generated for each B-scan, is used as an update clock of C-scan, and the C-scan trigger initiates spectral detection. Complete spectral signals and A-triggers for a single C-scan are stored in the on-board memory of the A/D board, then transferred to the main memory of a PXI PC unit after the measurement, and finally stored on a hard disk. The stored data is loaded during the post-processing process, and arranged into a three-dimensional spectral signal by using the A-scan triggers, this is followed by the application of the above-mentioned signal processing. A typical C-scan comprises 200 B-Scans, each of which comprises 200 A-scans. Hence, the volume size is $200 \times 200 \times 1024$ voxels and the acquisition time is 2 s.

Figure 7 shows three-dimensional tomographies of *in vivo* human anterior eye segments. Figures 7(a) and 7(b) show the entire structures of the human iris (IR) and cornea, respectively. The measurement ranges are 16.5 mm (horizontal), 16.5 mm (vertical), and 6.0 mm (depth). Figure 7(c) reveals the iridocorneal angle opening. In Fig. 7(d), the iridocorneal angle opening, crystalline lens, and nucleus lentis (NL) are evident. Trabecular meshwork (TM) and zonules of Zinn (ZZ), which are difficult to recognize in a two-dimensional OCT image, can be observed. Wavelike structures on the sclera which can be seen in the movies of Figs. 7(c) and 7(d) are motion artifacts, and could be eliminated by using a compensation algorithm. The measurement ranges of Figs. 7(c) and 7(d) are 6.1 mm (horizontal), 6.1 mm (vertical), and 6.0 mm (depth)

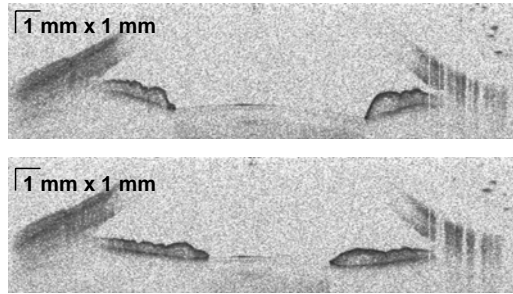


Fig. 8. B-scan images of human anterior eye chamber in dark room (upper) and bright room (lower). A tomographic movie shows contracting motion of the iris (1.9MB version and 5.2MB version).

5. Tomographic movie

In a tomographic movie mode, the galvano mirror for B-scan is driven by a triangular wave, and spectral signals are detected both on upward and downward slopes. Complete spectral signals and A-triggers for a tomographic movies are stored in the on-board memory of the A/D board, then transferred to the main memory of a PXI PC unit after the detection, and stored on a hard disk. A post processing program loads the stored signals, arranges each frame of the movie by using A-triggers and applies above-mentioned signal processing to the spectral signals for image formation.

Figure 8 shows a tomographic movie of an *in vivo* human anterior eye chamber. The measurement ranges are 20.3 mm (horizontal), and 5.9 mm (depth). A single B-scan image consists of 500 A-scans, and the movie comprises 80 B-scans. A single B-scan was acquired every 25 ms (40 frames/s), and the movie shows these B-scans with the frame rate of 20 frames/s. When the acquisition started, simultaneously a light bulb to illuminate the eye was turned on. The contracting motion of an iris by light illumination is shown in the movie.

6. Conclusions

We demonstrated the application of a 1.3 μm SS-OCT system to investigate *in vivo* human anterior eye segments. A ready-to-ship wavelength scanning light source has been employed for this purpose. The light source has a center wavelength of 1.31 μm , -3dB-scanning range of 110 nm, scanning rate of 20 KHz, and high linearity in frequency sweeping. The SS-OCT system is capable of displaying realtime two-dimensional OCT and obtaining a three-dimensional OCT volume with the measurement time of 2 s. A simple time-frequency calibration method, which does not require any additional equipment, e.g., a fiber Fabry-Perot and a high-speed oscilloscope, is presented.

In vivo human anterior eye segments are investigated two-dimensionally and three-dimensionally. The three-dimensional OCT volumes reveal the structures of the sample, which are difficult to recognize in two-dimensional OCT scans. A two-dimensional tomographic movie showed a contracting motion of a human iris by light illumination.

Acknowledgments

This research is partially supported by the Grant-in-aid for Scientific Research 15760026 from the Japan Society for the Promotion of Science (JSPS), Japan Science and Technology Agency, and the Special Research Project of Nanoscience at University of Tsukuba.

Shuichi Makita is supported by JSPS through a contract under the Promotion of Creative

Interdisciplinary Materials Science for Novel Functions, 21st Century Center of Excellence (COE) Program.